Elastic and inelastic scattering of $^{16}O+^{64}Zn$ at near-barrier energies

C. Tenreiro,* J. C. Acquadro, P. A. B. Freitas, and R. Liguori Neto
Universidade de São Paulo, IFUSP Laboratorio Pelletron, C.P. 20516-01498-970, São Paulo, Brazil

G. Ramirez and N. Cuevas
Departamento de Física, Facultad de Ciencias, Universidad de Chile, Casilla 653, Santiago 1, Chile

P. R. S. Gomes, R. Cabezas, and R. M. Anjos
Departamento de Física, Universidade Federal Fluminense, Av. Gal. Milton Tavares de Souza s/n, Niterói, R. J., 24210, Brazil

J. Copnell
University of Manchester, Physics Department, Schuster Laboratories, Manchester M13 9PL, United Kingdom
(Received 8 December 1995)

Elastic and inelastic scattering angular distributions were measured for the $^{16}O+^{64}Zn$ reaction at bombarding energies close to the Coulomb barrier. The experimental data were analyzed within the optical model and coupled-channel model. An extended dispersion relation of integral quantities using a Gaussian weight was applied, instead of the normal relationship. Within this frame, the optical model parameters obtained from the data are in agreement with the dispersion relation and show the threshold anomaly at energies close to the Coulomb barrier. Analysis of the inelastic scattering angular distributions leads to some indications that an inelastic threshold anomaly is beginning to develop at energies lower than the ones for which our data were taken. [S0556-2813(96)01106-5]

PACS number(s): 25.70.Bc, 24.10.Eq, 24.10.Ht

I. INTRODUCTION

The study of the energy dependence of the strength of the real and imaginary optical potentials which fit the elastic scattering data, especially at energies in the vicinity of the Coulomb barrier (V_b), has become quite common in recent years. Emphasis is usually given to the analysis of the so called threshold anomaly, which is the rapid variation of the real and imaginary potentials, observed as the energy decreases towards V_b. This fact and its connection with the dispersion relation that links the optical model depth parameters have been the subject of several works in different mass regions, such as, for example, on $^{16}O+^{208}Pb$ [1] and $^{16}O+^{60}Ni$ [2], where it was shown that the imaginary potential decreases sharply when the energy decreases to values below V_b, while the real potential increases, reaches a maximum value, and then decreases in a sort of bell shape.

In this paper a situation is presented where the dispersion relation has to be applied by taking into account the spatial localization where the sensitive radius is defined; this is necessary to apply the generalized dispersion relation [3] using volume integrals of the potentials, per interacting pair of nucleons, and properly weighted in order to include this spatial range. The dispersion relation is also expected to apply to all elements of the scattering matrix [4]; in particular, this should also be true for the inelastic scattering; if the threshold anomaly is observed in the elastic scattering, then a similar behavior is expected in the inelastic channel.

In the present work, elastic and inelastic scattering cross sections for the $^{16}O+^{64}Zn$ reaction were determined experimentally in the energy range $32.0 \leqslant E_{c.m.} \leqslant 51.2$ MeV. The elastic scattering data are analyzed via the optical model in order to find the energy dependence of the real and imaginary parts of the potentials which fit the data. For the inelastic channel, the real and imaginary parts of the transition potential are calculated by performing distorted-wave Born approximation (DWBA) analysis of the angular distributions; the presence of the threshold anomaly in this channel is discussed. A coupled-channel analysis is performed, where the structure of the target nucleus, such as the coupling of different channels, is considered in the calculation of elastic and inelastic differential scattering cross sections.

The excitation function for this system has been previously reported [5] at $\theta_{lab}=174°$.

II. EXPERIMENTS AND RESULTS

The ^{16}O beam extracted from a Duoplasmatron ion source was delivered by the 8UD 9 MV Tandem accelerator facility at the University of São Paulo. The beam intensity on the target was typically 120 nA, and the laboratory energy range at which the angular distributions were measured was from 40 to 64 MeV. Energy corrections for energy losses were taken into account. The Zn targets were made by evaporating Zn oxide by electron bombardment on a thin carbon backing (about 5 $\mu g/cm^2$ thick). The target thicknesses were within the 30 to 40 $\mu g/cm^2$ range. Three targets of Zn and a thin one of gold were mounted vertically at the center of the scattering chamber. The elastic and inelastic scattering data were obtained using an array of nine silicon surface barrier detectors with angular separation of 5° between them. The detectors are coupled to a device in front of them containing cir-

*Present address: Departamento de Física, Facultad de Ciencias, Universidad de Chile, Casilla 653, Santiago 1, Chile.

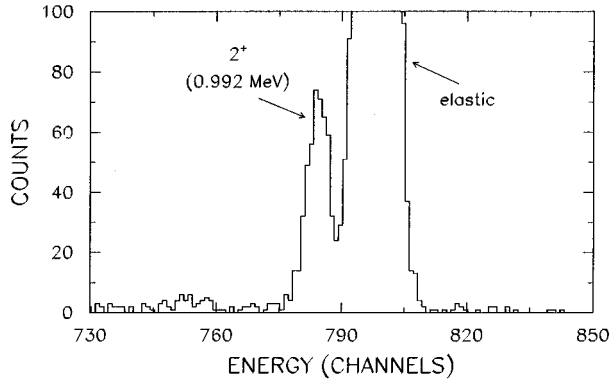

FIG. 1. Typical spectrum for the $^{16}O+^{64}Zn$ reaction, obtained at $E_{lab}=54.0$ MeV and $\theta_{c.m.}=40°$. The expanded region shows very clearly the elastic and the first inelastic (0.992 MeV) peaks.

cular slits for solid angle definition and antiscattering apertures. Two silicon surface barrier monitor detectors were mounted at $\pm 15°$ to the beam direction. The relative solid angle of the detectors was determined by the Rutherford scattering of ^{16}O on the gold target. The array was mounted on a circular plate inside the 1 m scattering chamber. Angle determination was made by reading on a goniometer with a precision of $\pm 0.05°$. The angular distributions were taken from $\theta_{c.m.}\sim 20°$ to $\sim 175°$, except for the higher energies where practical counting times become an important limiting factor.

Figure 1 shows a ^{16}O spectrum taken at $\theta_{lab}=40°$, for a bombarding energy in the laboratory frame of 54.0 MeV. Typical resolution obtained close to $\theta_{lab}\sim 90°$, which is the most unfavored case, was of the order of 350 keV [full width at half maximum (FWHM)]. The previous value is due mostly to energy loss and straggling of the ions emerging from the target and kinematic broadening. As can be seen from this figure, a very nice separation is obtained between the elastic and inelastic peaks, for the first 2^+ excited state in ^{64}Zn. The ratio to the Rutherford scattering was obtained assuming that cross sections measured at forward angles are pure Rutherford. The uncertainty of the experimental data goes from 5% at forward angles to 25% at the most backward ones.

III. OPTICAL MODEL ANALYSIS

The optical model analysis of the data was performed assuming potentials of the Woods-Saxon form, namely,

$$U(r)=V(r)+iW(r). \tag{1}$$

Both real and imaginary parts are defined by the usual parameters depth, radius, and diffuseness, V_0, r_{0v}, a_v and W_0, r_{0w} and a_w, respectively. The radial dependence of these parts is expressed in the form

$$U(r)=\frac{-V_0}{1+\exp[(r-R_v)/a_v]}-\frac{iW_0}{1+\exp[(r-R_w)/a_w]} \tag{2a}$$

where

$$R_v=r_{0v}(A_p^{1/3}+A_t^{1/3}) \quad \text{and} \quad R_w=r_{0w}(A_p^{1/3}+A_t^{1/3}). \tag{2b}$$

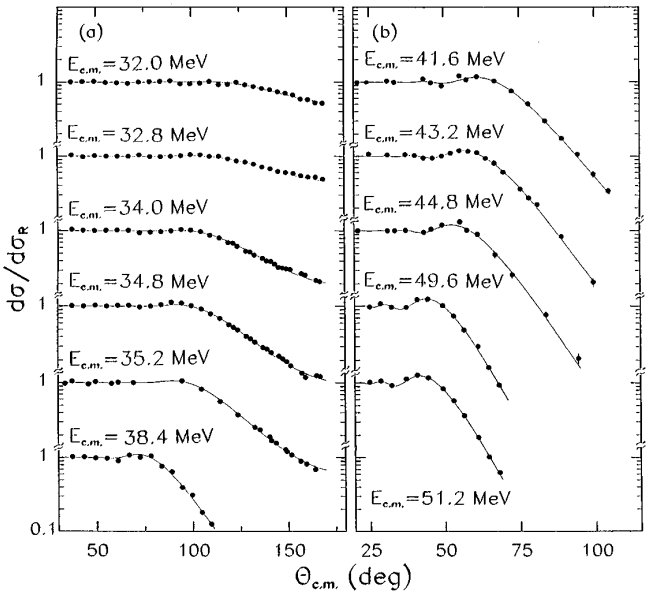

FIG. 2. Elastic scattering angular distributions for the $^{16}O+^{64}Zn$ reactions. The solid lines show the best fit within the optical model using the OMP parameters listed in Table I.

A_p and A_t denote the projectile and target mass numbers.

The fitting procedure of the data can be summarized as follows. First the optical model potential (OMP) parameters that reproduce the experimental elastic scattering angular distributions were determined. The code PTOLEMY [6] was used for such purpose and the selection criterion for the best fitting was the set that minimizes the χ^2, per degree of freedom N, defined as

$$\chi^2=\frac{1}{N}\sum_{i=0}^{N_{\text{points}}}\frac{(\sigma^i_{\text{theo}}-\sigma^i_{\text{exp}})^2}{\Delta\sigma^2_{\text{exp}}}. \tag{3}$$

The geometry of the system turned out to be $r_{0v}=r_{0w}=1.25$ fm and $a_v=a_w=0.56$ fm, for the real and imaginary parts. Very small deviations from these values were observed. Figure 2 shows the elastic scattering angular distributions for the whole energy range. Also on the same figure the best fit obtained with the OMP parameters from Table I is shown (solid line). An important feature of the optical model analysis is that the same experimental elastic scattering angular distribution can be fitted, with reasonable good χ^2 values, by more than one set of OMP parameters. However, it is found that the real parts of these OMPs have the same value at a certain radius, where they cross each other, which is called the sensitive radius or crossing radius. The experimental data for the elastic scattering was fitted in order to obtain the crossing radius. The values of r_{0v} and r_{0w} were kept fixed at 1.25 fm and the diffuseness $a_v=a_w$ was changed from 0.52 to 0.62 fm in steps of 0.02 fm, in order to find the V_0 and W_0 values that fit the data, using the best χ^2.

Table II shows the values for the real, R_{CV}, and imaginary, R_{CW}, crossing radius and the respective standard deviations σ. Figure 3 shows the crossing radius at the energy of $E_{c.m.}=34.8$ MeV. The 15 intersection points between the six sets of OMP parameters at each energy were found using a Newton-Ramphson routine. A well defined crossing radius

TABLE I. Summary of the potential parameters obtained from the optical model analysis of the elastic scattering angular distributions and deformation lengths βR obtained from the DWBA analysis, performed on the inelastic scattering angular distributions.

$E_{\text{c.m.}}$ (MeV)	V_0 (MeV)	a_v (fm)	W_0 (MeV)	a_w (fm)	$\beta_v R_v$ (fm)	$\beta_w R_w$ (fm)	χ^2
32.0	68.21	0.557	7.05	0.574	0.892	2.823	0.60
32.8	51.09	0.556	9.14	0.551	0.941	1.815	1.09
34.0	44.30	0.562	18.76	0.556	1.106	1.047	0.74
34.8	43.78	0.561	14.76	0.551	1.207	1.106	1.07
35.2	45.69	0.559	12.09	0.563	1.250	0.411	1.26
38.4	44.66	0.560	20.61	0.560	1.117	1.011	1.38
41.6	41.03	0.560	18.56	0.560	0.889	1.013	2.22
43.2	44.40	0.560	18.97	0.559	1.258	0.932	0.62
44.8	43.99	0.560	19.30	0.560	1.258	0.831	1.20
49.6	46.82	0.561	17.43	0.554	1.106	1.359	1.07
51.2	43.52	0.561	19.40	0.552	1.106	1.334	0.82

can be seen from this figure for the real part of the OMP, with $\sigma=0.02$ fm. However, for the imaginary part, the intersecting points are more scattered, with an average value for R_{CW} of 9.86 fm and a standard deviation of $\sigma=0.12$ fm. It can be seen that the crossing radii for the real part of the potential are not necessarily equal to the ones obtained for the imaginary part of the potential. The R_{CV} values increase with energy and the opposite is observed with the R_{CW} ones. Such an energy dependence has already been reported for the $^{16}O+^{208}Pb$ system, where a systematic increase from 12.5 to 13.0 fm is observed when the bombarding energy goes from 80 to 100 MeV [7]. This behavior of R_{CV} could be a direct consequence of the variation of the real potential at energies close to the threshold anomaly, as predicted from the dispersion relation.

The physical meaning of the crossing radius has already been studied and it is associated with the point at which the OMP is well defined by the elastic scattering data [8]. However, the analysis of the experimental data for the $^{16}O+^{208}Pb$ system shows that the value of the crossing radius depends strongly on the shape of the nuclear potential [9] and, therefore, the dispersion relation cannot be evaluated directly from values of the potentials at just one point.

TABLE II. Real and imaginary crossing radii $R_C R$ and $R_C W$ and their standard deviations σ.

$E_{\text{c.m.}}$ (MeV)	R_{CV} (fm)	σ (fm)	R_{CW} (fm)	σ (fm)
32.0	10.35	0.06	10.68	0.22
32.8	10.13	0.09	10.04	0.13
34.0	10.39	0.09	10.66	0.06
34.8	10.38	0.03	9.86	0.12
35.2	10.42	0.03	9.64	0.26
38.4	10.92	0.10	9.76	0.34
41.6	10.84	0.02	9.78	0.08
43.2	10.70	0.01	9.76	0.10
44.8	10.72	0.23	9.65	0.10
49.6	10.67	0.13	9.04	0.12
51.2	10.69	0.01	9.33	0.22

IV. ENERGY DEPENDENCE OF THE POTENTIALS

The energy dependence of the real and imaginary parts, $V(r;E)$ and $W(r;E)$, without taking into account nonlocality effects, are expected to be given by the dispersion relation [3] which arises from considerations of causality. According to Ref. [3], the dispersion relation between the real and imaginary parts of the OMP can be written as

$$\Delta V(r;E)=\frac{\mathrm{P}}{\pi}\int\frac{W(r;E')}{E'-E}\,dE', \tag{4}$$

where P denotes the principal value and

$$\Delta V(r;E)=V(r;E)-V_0. \tag{5}$$

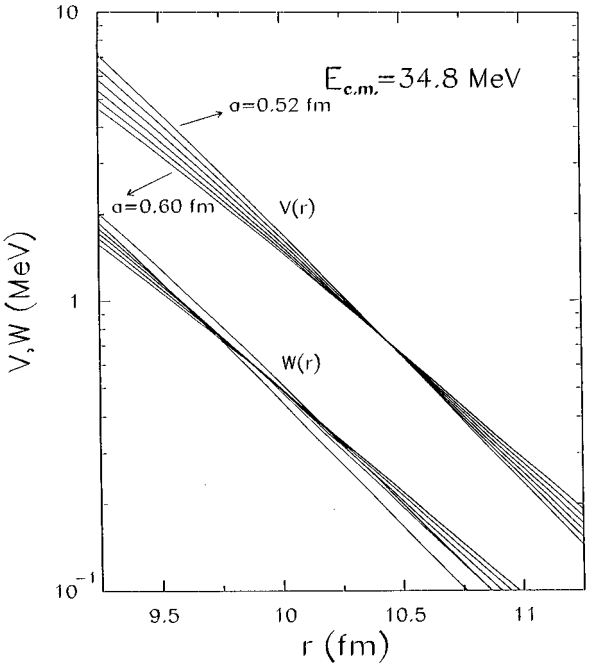

FIG. 3. $V(r)$ and $W(r)$ versus r for different values of the real and imaginary diffuseness parameters. Crossing radius determination for $E_{\text{c.m.}}=34.8$ MeV.

V_0 is the energy-independent term. In order to calculate the energy dependence of the real and imaginary parts of the OMP and their connection through the dispersion relation (4), we have followed the procedure introduced by Brandan *et al.* [10] for the analysis of the elastic scattering of the ^{58}Ni+^{27}Al system.

Following Refs. [3] and [10], the dispersion relation (4) can be expressed as

$$\Delta[G(E)]_V=\frac{\mathrm{P}}{\pi}\int\frac{[G(E')]_W}{E'-E}\,dE', \tag{6}$$

where

$$[G(E)]_V=\frac{1}{A_pA_t}\int V(r;E)G(r)4\pi r^2dr \tag{7}$$

and

$$[G(E)]_W=\frac{1}{A_pA_t}\int W(r;E)G(r)4\pi r^2dr. \tag{8}$$

In these equations the weighting function has been defined as a Gaussian centered on some mean value of the crossing radius R_g, and with a width σ defined in such a way that it considers the region where the OMP is sensitive to the elastic scattering data. According to this, $G(r)$ is expressed as

$$G(r)=\frac{1}{\sqrt{2\pi}\sigma}\exp\left[-\frac{(r-R_g)}{2\sigma^2}\right]. \tag{9}$$

Figure 4 shows the values of $[G(E)]_V$ and $[G(E)]_W$ calculated with the OMP parameters from Table I and making R_g=10.4 fm and σ=0.5 fm. The error bars reflect the uncertainties in the OMP parameters that are obtained if χ^2 increases by one unit, according to the code PTOLEMY. We have taken the integral limits in (7) and (8) in such a way that the values of the crossing radius do not present a dispersion around R_g larger than the mean wavelength ($\sigma\leqslant\lambda/2$). Values of R_g between 10.2 and 10.5 fm, used in the evaluation of $G(r)$, imply only modifications that are qualitatively small in the behavior of $[G(E)]_V$ and $[G(E)]_W$ with energy, mainly due to the fact that the radial dependence of the real and imaginary parts of the OMP that fit the data are not much different between them and they do not vary too much in the whole region of energy that has been studied. The curves for $[G(E)]_V$ shown in Fig. 4 were obtained using the dispersion relation for the indicated parametrizations of $[G(E)]_W$, normalized to the empirical value of $[G(E)]_V$ near the energy $E_{\mathrm{c.m.}}$=38.4 MeV. Some features from the optical model analysis of the elastic scattering can be delineated: the quantity $[G(E)]_W$, which is related to the absorptive OMP, seems to show a plateau at higher energies, like the one obtained for ^{16}O+^{208}Pb [1], but it decreases slightly as the energy increases. Also, at energies close to V_b, a sort of pocket is observed with its higher value at the lower-energy side just below V_b, and after that $[G(E)]_W$ decreases sharply. The energy dependence of the quantity $[G(E)]_V$, connected with the real OMP, is in qualitative agreement

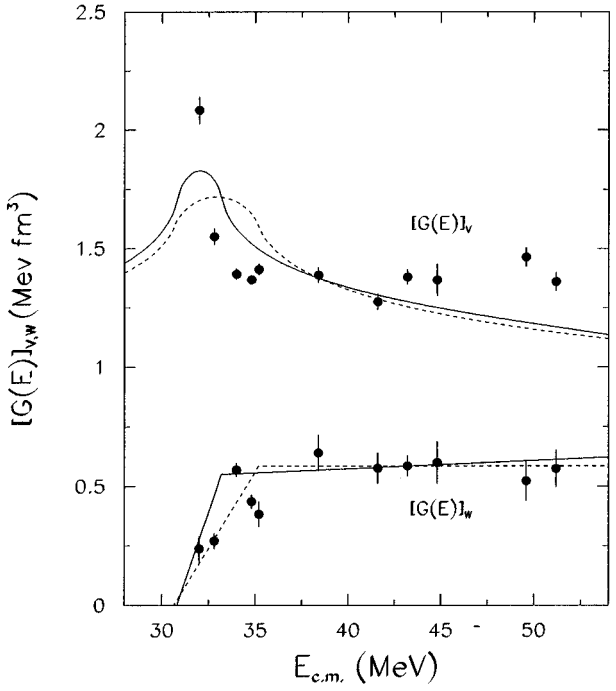

FIG. 4. Variation with energy of $[G(E)]_V$ and $[G(E)]_W$ defined in the text. Two different parametrizations for $[G(E)]_W$ are shown with the corresponding curves obtained for $[G(E)]_V$.

with the dispersion relation and increases its magnitude at $E_{\mathrm{c.m.}}$=32.0 MeV, where the threshold anomaly is observed.

At this lowest energy, a detailed analysis of the OMP parameters that fit the experimental data has been performed. The result is summarized in Table III. These OMP parameters were obtained by imposing in the search the following conditions: the ones marked with $*$ were kept fixed, and the rest were left to change freely. Also the values marked with $+$ might vary, but were restricted to be the same for the real and imaginary parts of the potential. The last condition was necessary to avoid getting values for a_w and r_{0w} out of the range with a reasonable physical meaning. All the OMP parameters gave equally good fittings of the data, but the most interesting fact is that the values obtained for $[G(E)]_V$ are coincident, within error, with $[G(E)]_V$=2.0 MeV fm^3, which is greater than the values obtained for the higher energies. The values of $[G(E)]_W$, from Table III, are more fluctuating, but all of them are under the plateau defined for higher energies. The energy dependence of the quantity $[G(E)]_V$ is in qualitative agreement with the dispersion relation and shows a sharp increase of magnitude at $E_{\mathrm{c.m.}}$=32.0 MeV, where there is a threshold anomaly.

V. INELASTIC SCATTERING ANALYSIS

A. DWBA calculation

The angular distributions measured for the inelastic scattering ^{64}Zn(^{16}O,^{16}O)^{64}Zn(2^+; 0.992 MeV) were fitted by performing DWBA calculations and using the collective model to determine the shape of the transition potential. The DWBA calculations were also performed using the code PTOLEMY. In this way, the transition potential is given by the derivative of the OMP

TABLE III. Different sets of OMP parameters that fit the experimental data and their corresponding functions $[G(E)]_V$ and $[G(E)]_W$ defined in Eqs. (7) and (8). $E_{\text{c.m.}}=32.0$ MeV.

V_0 (MeV)	r_{0v} (fm)	a_v (fm)	W_0 (MeV)	r_{0w} (fm)	a_w (fm)	χ^2	$[G(E)]_V$ (MeV fm^3)	$[G(E)]_W$ (MeV fm^3)
67.1	1.25*	0.56*	7.90	1.25*	0.56*	0.61	2.08±0.06	0.25±0.06
58.7	1.25*	0.58*	6.77	1.25*	0.58*	0.63	2.04±0.05	0.24±0.05
52.1	1.25*	0.60*	5.80	1.25*	0.60*	0.63	2.01±0.05	0.22±0.05
46.7	1.25*	0.62*	4.97	1.25*	0.62*	0.66	1.99±0.05	0.21±0.04
77.6	1.25*	0.54*	9.21	1.25*	0.54*	0.65	2.14±0.06	0.25±0.07
43.5*	1.254$^+$	0.626	7.50*	1.254$^+$	0.575	0.67	1.98±0.07	0.26±0.04
43.5*	1.208	0.726$^+$	7.50*	1.111	0.726$^+$	0.64	2.01±0.07	0.15±0.04
43.5*	1.267$^+$	0.608	18.0*	1.267$^+$	0.460	0.71	2.07±0.07	0.35±0.07
43.5*	1.208	0.727$^+$	15.0*	1.031	0.727$^+$	0.64	2.01±0.07	0.15±0.04
35.64	1.200*	0.806$^+$	1.85	1.200*	0.806$^+$	0.62	2.08±0.04	0.11±0.03
18.28	1.300*	0.771	2.69	1.200*	0.806*	0.60	2.04±0.03	0.16±0.04
25.85	1.300*	0.642$^+$	2.62	1.300*	0.642$^+$	0.61	1.95±0.04	0.20±0.03
25.04	1.336$^+$	0.560*	3.23	1.336$^+$	0.560*	0.64	1.97±0.05	0.25±0.06

$$U_{\text{tr}}(r)=V_{\text{tr}}(r)+iW_{\text{tr}}(r)=\beta_v R_v\frac{\partial V}{\partial r}+i\beta_w R_w\frac{\partial W}{\partial r} \quad (10)$$

where $\beta_v R_v$ and $\beta_w R_w$ are the real and imaginary deformation lengths, respectively, for $L=2$. The Coulomb deformation length was kept fixed and derived from

$$\beta_C R_C=\frac{4\pi|B(EL)|^{1/2}}{3ZeR_C}. \quad (11)$$

In Eqs. (10) and (11), R_v and R_w are given in Eq. (2b) and $R_C=r_{0C}(A_p^{1/3}+A_t^{1/3})$.

In order to fit the experimental data the values of $\beta_v R_v$ and $\beta_w R_w$ were varied independently, keeping the radial shape of V_{tr} and W_{tr} unchanged.

In the calculations, the OMP's in the entrance and exit channels were considered to be the same, except for $E_{\text{c.m.}}=32.8$ MeV, where for the exit channels we have used the values obtained for the OMP parameters that fit the elastic scattering data at $E_{\text{c.m.}}=32.0$ MeV (solid line in Fig. 7 below). This case will be discussed separately below. The angular distributions for the inelastic scattering and the predictions from the DWBA calculations are shown in Figs. 5–7. Table I shows the values obtained for $\beta_v R_v$ and $\beta_w R_w$ from the fitting procedure.

It can be seen that for energies above $E_{\text{c.m.}}=34$ MeV good agreement between DWBA predicted cross sections and the experimental data is achieved. The real part of the transition potential can be fitted with reasonable precision. On the other hand, the imaginary part of the transition potential W_{tr} is less sensitive as the energy decreases. Figure 6 shows for $E_{\text{c.m.}}=34.8$ MeV (dashed line) a variation of 20% in the value of V_{tr} and for $E_{\text{c.m.}}=35.2$ MeV, also with dashed line, is shown a variation of 50% in W_{tr}. For energies below $E_{\text{c.m.}}=34$ MeV, it was not possible to reproduce the experimental angular distributions. This can be seen in Fig. 7 for the energies $E_{\text{c.m.}}=32.0$ and 32.8 MeV, where the DWBA prediction only reproduces the data up to the Coulomb-nuclear interference region and does not reproduce the further increase of the inelastic cross section at backward angles. For $E_{\text{c.m.}}=32.8$ MeV is shown in Fig. 7, with a dashed line, the DWBA calculation where the same OMP's for the entrance and exit channels were used. This is the only case where a significant difference is observed by doing this type of variation in the DWBA. The calculation of V_{tr} and W_{tr} in this energy region, which could reproduce the increase of the inelastic cross section at backward angles, results in a shift of the position of the minima in the angular distribution, due to the Coulomb-nuclear interference, of more than 10° towards lower angles and, being so, the rest of the angular distribution is not reproduced. A similar situation was ob-

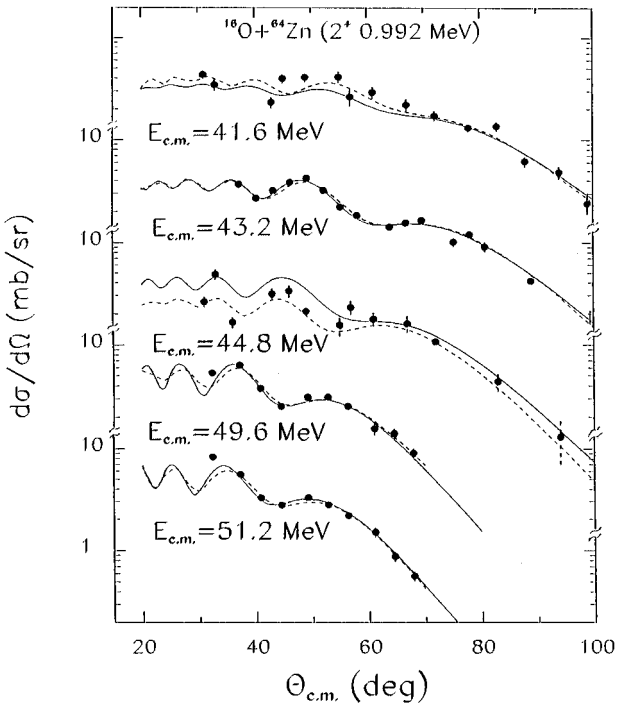

FIG. 5. Inelastic scattering angular distributions for the first 2^+ excited state in ^{64}Zn, at 0.992 MeV. Solid lines represent the best fit obtained from the DWBA analysis of the data. See text for explanation of dashed lines.

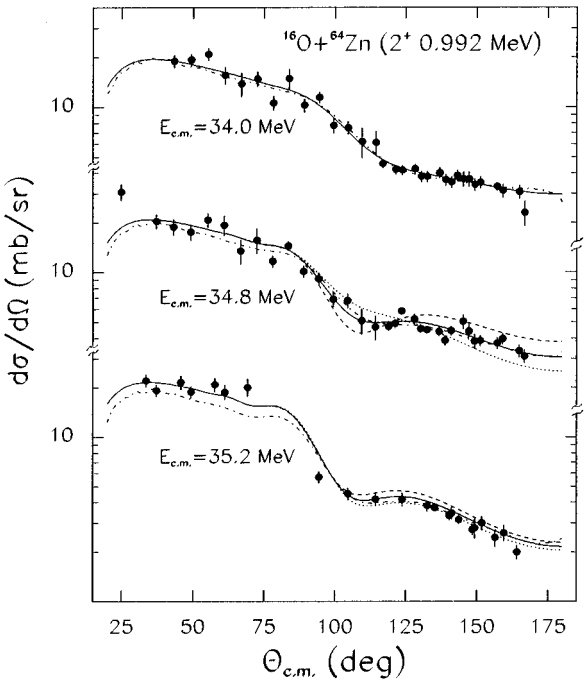

FIG. 6. Like Fig. 5; see the text for explanation of the dotted and dashed lines.

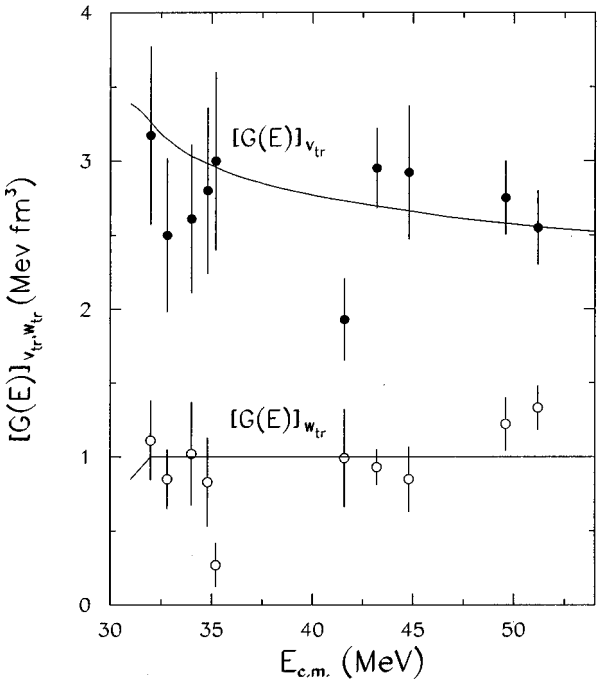

FIG. 8. Variation with energy of the $[G(E)]_{V_{tr}}$ and $[G(E)]_{W_{tr}}$ values obtained from the DWBA analysis.

served in the analysis of the inelastic scattering of ^{208}Pb(^{16}O, ^{16}O)^{208}Pb(3^-) within the framework of the collective model [11]. In this case the inelastic data could not be fitted at near-barrier energies where the threshold anomaly in the elastic scattering is observed.

The results for the inelastic scattering data are summarized in Fig. 8. In this figure the volume integral of the real and imaginary parts of the transition potential is shown weighted by a Gaussian function given by (9) with R_g=10.4 fm and σ=0.5 fm, plotted as a function of the incident energy. This result does not indicate that the inelastic threshold anomaly is present for the ^{16}O+^{64}Zn system, in the region of energy studied in this work. However, Gómez-Camacho and Nagarajan [12] have shown that the threshold anomaly for the inelastic scattering will be shifted to lower energies by an amount $(a/R)V_b$ relative to that in the elastic channel. For the system studied here a crude estimate of this shift, using a=0.57 fm, R=10.0 fm, and V_b=34.48 MeV, indicates that the inelastic threshold anomaly occurs at an energy of ~32 MeV, which is below our lowest energy value. This prediction, and the fact that angular distributions of inelastic scattering at the lowest energies were not reproduced by our calculations, within the collective model, is an indication that the inelastic threshold anomaly is beginning to rise and this can be answered only with a further extension of the data to lower energies.

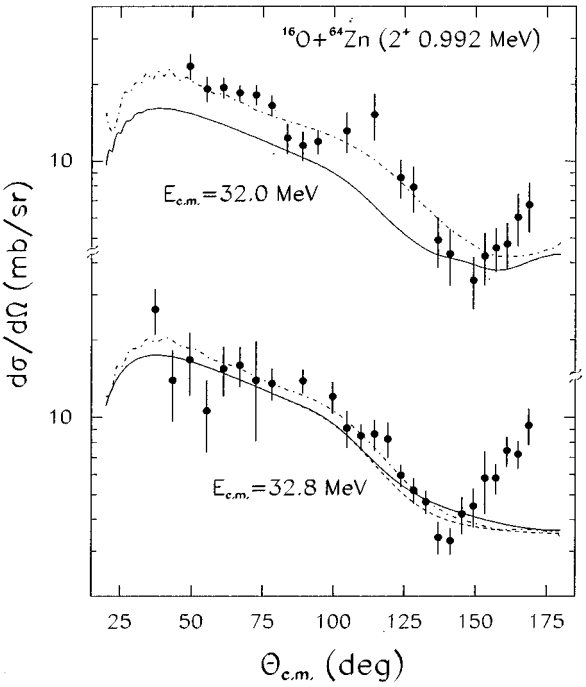

FIG. 7. Like Fig. 5; see the text for the explanation of the dashed and dot-dashed lines.

B. Coupled-channel analysis

In order to analyze in more detail the possible influence of the structure of the low-lying collective levels of the target nucleus and the effect of channel coupling at lower energies on the inelastic angular distribution, a coupled-channel analysis was performed.

Elastic and inelastic scattering studies on Zn isotopes indicate the possibility of an oblate to prolate transition between N=36 and 46 [13]. In Ref. [14] it has been found that ^{64}Zn and ^{66}Zn have a prolate shape in the first excited state. Ballester, Casal, and England [15] have concluded that a transition in the nuclear structure occurs between ^{64}Zn and ^{66}Zn for the γ band. In this sense, on account of their softness characteristic, in the analysis of inelastic data different collective models have been used to describe the structure of

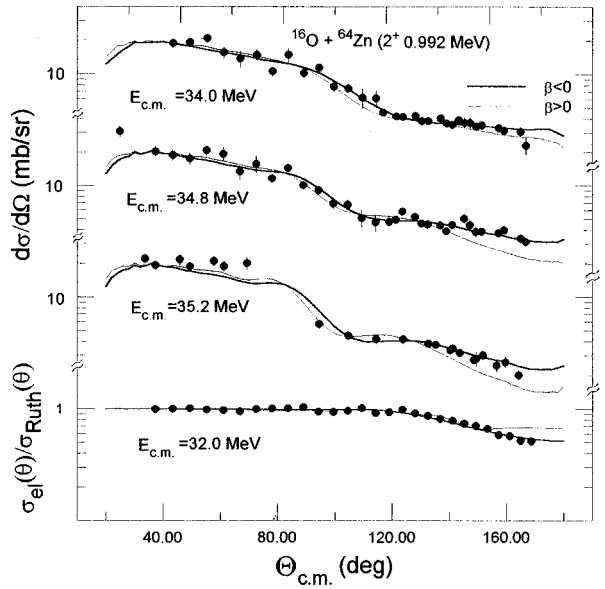

FIG. 9. Comparison of the coupled-channel calculation of elastic and inelastic angular distributions at positive and negative values of β_2.

the even isotopes of zinc [16–23].

In our coupled-channel analysis, the first step was the inclusion of excitation to and reorientation of the first excited state of ^{64}Zn at 0.992 MeV using the coupled-channel code ECIS [24], which has the possibility of considering different collective models. The coupling strength for reorientation of the 2^+ excited state of ^{64}Zn was assumed to be equal to that for the $0^+ \leftrightarrow 2^+$ coupling. Before starting a complete analysis of the data, we tested three different collective models for the two lowest incident energies: the harmonic vibrational model (HVM) [25], the symmetric rotational model (SRM) [26], and the asymmetric rotational model (ASM) [27]. In a preliminary fitting of the data we found that the SRM best describes the experimental angular distributions.

On this basis, the calculations assume the 0^+ and 2^+ states to be members of a ground-state rotational band having $K=0$. Coulomb corrections to the scattering were included in the calculations. To explore the sign of the quadrupole deformation parameter β_2, searches were performed using starting values of β_2 equal to both -0.23 and $+0.23$. In both cases, the starting parameters were the set in Table I.

Calculations demonstrate that the elastic and inelastic scattering differential cross sections at the higher energies ($E_{\text{c.m.}}=41.6$ MeV and above) are relatively insensitive to the sign of β_2. However, at lower energies the situation changes. At $E_{\text{c.m.}}=32.0$ MeV, the sign of β_2 is particularly sensitive to the backward part of the elastic angular distribution (see the dashed line in Fig. 9), and at energies just above the barrier this sensibility is most pronounced in the inelastic channel. In general, the inelastic scattering differential cross sections are best reproduced by calculations having negative β_2.

The parameter set of Table I, derived from the optical model analysis of the elastic scattering, was used as the starting point of a search to simultaneously adjust the differential cross section data for scattering to the ground and first excited states of ^{64}Zn. An initial series of χ^2 searches was done, where the radii of the real, imaginary, and Coulomb potentials r_{0v}, r_{0w}, and r_{0C} were varied, keeping fixed the depth of the potential and its diffusenesses. The quadrupole deformation parameter was initially fixed at the value of -0.23 for all the potentials. Then a second series of three-parameter fits was performed by varying the deformation parameters β_{2v}, β_{2w}, and β_{2C}, separately, for the three potentials. A third series of fits was finally performed by varying the depth of the real and imaginary potentials, V_0 and W_0, using a coupling scheme of four states: 0^+-2^+-4^+-6^+. The resulting potential parameters obtained from the search are listed in Table IV, together with the χ^2 values.

The coupled-channel angular distributions for the elastic differential cross section and the inelastic one, at energies above the barrier, were close to the ones obtained in Figs. 5 and 6 (dotted lines) by DWBA analysis. At lower energies ($E_{\text{c.m.}}=32.0$ and 32.8 MeV), although the coupled-channel calculations (dot-dashed lines) were in better agreement than the DWBA calculations (full lines) for the inelastic angular distribution, as is shown in Fig. 7, it is still not possible to reproduce satisfactorily the structure observed in the data, such as the increase of the cross section at large angles. This structure, appearing at lowest energies in the backward angular distributions, was also previously noticed at the thresh-

TABLE IV. Summary of the OMP parameters obtained after a coupled-channel search, starting from the values given in Table I. The diffusenesses were kept the same as the ones obtained in the optical model analysis.

$E_{\text{c.m}}$ (MeV)	V_0 (MeV)	W_0 (MeV)	$\beta_v R_v$ (fm)	$\beta_w R_w$ (fm)	$\beta_C R_C$ (fm)	$\chi^2(0^+)$	$\chi^2(2^+)$
32.0	42.93	0.425	1.502	1.158	1.939	0.57	1.13
32.8	42.84	3.840	2.068	2.115	1.859	0.95	2.77
34.0	44.03	19.80	1.806	1.651	1.795	0.42	0.94
34.8	43.88	14.89	1.663	2.644	1.741	0.81	1.77
35.2	45.66	18.75	1.826	1.146	1.782	1.86	2.07
38.4	42.37	21.36	1.626	1.512	1.891	1.07	
41.6	39.02	22.79	1.517	1.379	1.872	2.32	2.22
43.2	39.87	19.63	1.898	1.696	1.804	1.85	2.67
44.8	41.29	18.88	1.264	2.191	1.620	2.02	2.57
49.6	47.01	16.47	1.777	2.243	1.790	1.71	3.36
51.2	42.93	18.89	1.731	2.082	1.785	1.50	1.96

old in other systems [28,29] and its nature is still unclear. In our case, it could not be described by the three collective models considered, nor by the coupling of different channels. These results could be improved by considering in a more realistic way the structure of the collective low-lying states of the ^{64}Zn isotope, which is still unclear.

Comparing the values of the real part of the potential depth obtained between DWBA and coupled-channel analyses from Tables I and IV, it is noted that as more inelastic channels are included, the need for a large value of V_0 for describing the data is reduced. This is another indirect indication, as pointed out by Satchler [30], of the existence of the threshold anomaly.

VI. SUMMARY AND CONCLUSIONS

The experimental elastic and inelastic scattering angular distributions were measured for $^{16}O+^{64}Zn$ from energies below the Coulomb barrier ($V_b^{\text{c.m.}}=34.48$ MeV) up to $\sim$1.8 times V_b. Optical model analysis of the elastic scattering angular distributions shows well defined crossing radii for the real and imaginary potentials, corresponding to common values for different families of OMP parameters which fit the data. These sensitive radii were found to have different spatial localization for the real and imaginary potentials.

An extended dispersion relation of the integral quantities $[G(E)]_V$ and $[G(E)]_W$ was used in the analysis of both elastic and inelastic scattering data, instead of the usual dispersion relation. The energy dependence of the integral quantities for the elastic scattering data is in qualitative agreement with the dispersion relation, and $[G(E)]_V$ increases its magnitude at the lowest energies, where the threshold anomaly is observed.

The inelastic scattering data can be fitted by a DWBA analysis for energies above the Coulomb barrier, but not for the low-energy data backward angles. The volume integrals of the real and imaginary parts of the transition potential do not show the energy dependence observed for the elastic channel. This is understood as due to a shift towards lower energies of the inelastic threshold anomaly, when compared with the elastic. For the lowest studied energy there are indications that the inelastic threshold anomaly is beginning to develop, but one needs to extend the measurements to further lower energies, in order to verify that.

The quality of the fits of elastic and inelastic data by coupled-channel and DWBA analyses was similar for energies above the barrier, and much better for the coupled-channel calculation at lowest energies, although the inelastic data at backward angles could not yet be reproduced.

ACKNOWLEDGMENTS

It is a pleasure to thank M. A. Nagarajan for enjoyable and useful discussions about these matters. This project has been partially financed by FAPESP (Fundação de Amparo à Pesquisa do Estado de São Paulo), and FONDECYT-Chile (Fondo Nacional De investigación Científica Y Tecnológica) by Contract No. 1940229. C.T., R.L.N., P.R.S.G., R.C., and R.M.A. thank CNPq (Conselho Nacional de Desenvolvimento Cientifico e Tecnologico, Brazil) for financial support. R.C. also thanks CLAF (Centro Latino Americano de Fisica) for financial support.

[1] M. A. Nagarajan, C. Mahaux, and G. R. Satchler, Phys. Rev. Lett. **54**, 1136 (1985).
[2] B. R. Fulton, D. W. Banes, J. S. Lilley, M. A. Nagarajan, and I. J. Thompson, Phys. Lett. **162B**, 55 (1985).
[3] C. Mahaux, H. Ngô, and G. R. Satchler, Nucl. Phys. **A449**, 354 (1986).
[4] G. R. Satchler, Nucl. Phys. **A472**, 591 (1987).
[5] S. Salem-Vasconcelos, E. M. Takagui, M. J. Bechara, K. Koide, O. Dietzsch, A. Bairrio Nuevo, Jr., and H. Takai, Phys. Rev. C **50**, 927 (1994).
[6] M. H. Macfarlane and S. C. Pieper, Argonne National Laboratory Report No. ANL-76-11, 1978 (unpublished).
[7] F. Vidabaek, R. B. Goldstein, L. Grodzins, S. G. Steadman, T. A. Belote, and J. D. Garret, Phys. Rev. C **15**, 954 (1977).
[8] H. Wojciechowski, N. B. Tannous, R. H. Davis, D. Stanley, M. Golin, and F. Petrovich, Phys. Rev. C **17**, 2126 (1978).
[9] M. H. Macfarlane and S. C. Pieper, Phys. Lett. **103B** 169 (1981).
[10] M. E. Brandan, J. R. Alfaro, A. Menchaca-Rocha, J. Gómez del Campo, G. R. Satchler, P. H. Stelson, H. T. Kim, and D. Shapira, Phys. Rev. C **48**, 1147 (1993).
[11] M. J. Smithson, J. S. Lilley, M. A. Nagarajan, P. V. Drumm, R. A. Cunningham, B. R. Fulton, and I. J. Thompson, Nucl. Phys. **A517**, 193 (1990).
[12] J. Gómez-Camacho and M. A. Nagarajan, Phys. Lett, B **300**, 303 (1993).
[13] D. Ardouin, R. Tamisier, M. Vergnes, G. Rotbard, J. Kalifa, G. Berrier, and B. Grammaticos, Phys. Rev. C **12**, 1745 (1975).
[14] R. Neuhausen, Nucl. Phys. **A282**, 125 (1977).
[15] F. Ballester, E. Casal, and J. B. A. England, Nucl. Phys. **A490**, 245 (1988), and references therein.
[16] J. Jabbour, L. H. Rosier, B. Ramstein, R. Tamisier, and P. Avignon, Nucl. Phys. **A464**, 260 (1987).
[17] P. J. Van Hall, J. F. A. G. Ruly, J. Krabbenborg, W. H. L. Moonen, and H. Offermans, in *Polarization Phenomena in Nuclear Physics*, edited by G. G. Ohlson, R. E. Brown, N. Jarmie, W. W. McNaughton, and G. M. Hale, AIP Conf. Proc. No. 69 (AIP, New York, 1981), p. 514.
[18] W. H. L. Moonen, P. J. Van Hall, S. S. Klein, G. J. Nijgh, C. W. A. M. Van Overveld, R. M. A. L. Petit, and O. J. Poppema, in Proceedings of the International Conference on Nuclear Structure, 1982, Vol. 1, p. 140.
[19] M. J. Throop, Y. T. Cheng, A. Goswami, O. Nalcioglu, D. K. McDaniels, L. W. Swenson, Nelson Jarmie, J. H. Jett, P. A. Lovoi, D. Stupin, Gerald G. Ohlsen, and G. C. Salzman, Nucl. Phys. **A283**, 475 (1977).
[20] E. Fabrici, S. Micheletti, M. Pignanelli, F. G. Resmini, R. De Leo, G. DeErasmo, and A. Pantaleo, Phys. Rev. C **21**, 844 (1980).
[21] G. Duhamel, L. Marcus, H. Langevin-Joliot, J. P. Didelez, P. Narbori, and C. Stephan, Nucl. Phys. **A174**, 485 (1971).

[22] L. F. Hansen, J. L. Kammerdierner, and M. S. Weiss, Phys. Rev. C. **4**, 1189 (1971).
[23] T. B. Robinson and V. R. W. Edwards, Nucl. Phys. **A301**, 36 (1978).
[24] J. Raynal, ECIS computer code (unpublished).
[25] T. Tamura, Rev. Mod. Phys. **37**, 679 (1965).
[26] J. M. Eisenberg and W. Greiner, *Nuclear Theory, Vol. I, Nuclear Models* (North-Holland, Amsterdam, 1970) p. 156.
[27] A. S. Davydov and G. F. Filippov, Nucl. Phys. **8**, 237 (1958).
[28] A. M. Stefanini, A. Tivelli, G. Montagnoli, D. R. Napoli, D. Bonamini, S. Beghini, F. Scarlassara, F. Soramel, C. Signorini, A. DeRosa, G. Inglima, M. Sandoli, G. Cardella, M. Papa, and F. Rizzo, Phys. Rev. C **41** 1018 (1990).
[29] A. M. Stefanini, D. Bonamini, A. Tivelli, G. Montagnoli, G. Fortuna, Y. Nagashima, S. Beghini, C. Signorini, A. DeRosa, G. Inglima, M. Sandoli, G. Cardella, and F. Rizzo, Phys. Rev. Lett. **59**, 2852 (1987).
[30] G. R. Satchler, Phys. Rep. **199**, 147 (1991).